

36 Introduction

37 The Tibetan Plateau (TP), which resembles a "third pole" and a "world water
38 tower", plays an important and special role in the global climate and energy–water
39 cycle (Xu et al., 2008; Wu et al., 2015). The TP covers a quarter of China.
40 Additionally, the average altitude of the TP is 4000 meters, reaching 1/3 of the
41 tropopause height, so it is called the "World Roof". Cumulus convection over the TP
42 transfers heat, moisture and momentum into the free troposphere, which can impact
43 the atmospheric circulation regionally and globally (Li and Zhang, 2016; Xu et al.,
44 2014) and reveals the important "window effect" for the transfer and exchange of
45 global energy and water vapor over the TP. It is a dynamic effect caused by the special
46 heat source that constitutes the "window effect" and "thermally driven" mechanism
47 over the TP.

48 The results of the second Tibetan Plateau Experiments (TIPEX II), which were
49 carried out in 1998, show that the strong convective plumes within PBL observed by
50 sodar and a frequently occurred deep mixed layer (>2 km) can lead to ubiquitous
51 "popcorn-like" cumulus clouds in Dangxiong, as proposed by Zhou et al. (2000), and
52 Xu et al. (2002) came up with a comprehensive physical pattern of land-air dynamic
53 and thermal structure on the TP (Xu et al., 2002; Zhou, 2000). The previous studies
54 have done many valuable researches on the triggering mechanism of moist convection
55 over moist and dry surfaces based on atmospheric observations and simulations (Ek
56 and Mahrt, 1994; Findell and Eltahir, 2003; Gentine et al., 2013). For dry surface, the
57 weak stratification and strong sensible heat flux result in the rapid growth of PBLH so
58 that the relative humidity at the top of the boundary layer RH_{top} increases rapidly,
59 which favors the formation of clouds. For moist surface, strong stratification and
60 evaporation (small bowen ratio) not only cause slow growth of PBLH but also
61 increase the mixed layer specific humidity and RH_{top} , which favor the formation and
62 development of clouds. Taylor et al. (2012) found that the afternoon rain falls
63 preferentially over soils that are relatively dry compared to the surrounding area,
64 especially for semi-arid regions. Guillod et al. (2015) reconciled spatial and temporal
65 soil moisture effects on the afternoon rainfall. They showed that afternoon
66 precipitation events tend to occur during wet and heterogeneous soil moisture
67 conditions, while being located over comparatively drier patches. Tuttle et al. (2016)
68 showed the empirical evidence of contrasting soil moisture–precipitation feedbacks
69 across the United States, and they found that soil moisture anomalies significantly
70 influence rainfall probabilities over 38% of the area with a median factor of 13%.
71 Findell et al. (2003) analyzed the model results over dry and wet soils in Illinois. They
72 summarized the predictive capability of rain and shallow clouds by using the
73 convective triggering potential (CTP) and a low-level humidity index, with HI_{low} as
74 measures of the early morning atmospheric setting. Our previous studies pointed out
75 that the developments of these cumulus clouds are related to the special large scale
76 dynamic structure and turbulence within PBL over the TP (Xu et al., 2014; Wang et al.,
77 2020). In addition, Wang et al., (2020) pointed out that, despite the same relative
78 humidity between eastern China and the TP, the lower temperature over the TP results

79 in a lower lifting condensation level. With the same surface sensible heat flux, lower
80 air density over the TP results in a larger buoyancy flux and a deeper boundary layer.
81 All the above results indicate the topography of the TP plays a major role in
82 increasing the occurrence frequency of strong convective clouds (Luo et al., 2011).
83 This conclusion is consistent with the viewpoint of Flohn (1967) who emphasized the
84 chimney effect of the huge cumulonimbus clouds on heat transfer in the upper
85 troposphere.

86 The TP is one of the regions in China that is featured with high frequency of
87 cumulus clouds, and the development of a cumulus system is related to both the
88 turbulence and special dynamical structure in the PBL over the TP. The vertical
89 motion over the TP is associated with anomalous convective activities. However, as
90 Li and Zhang (2016) mentioned, the details of PBL processes are not very clear. The
91 same is true for the diurnal variations and formation mechanism of low clouds over
92 the TP and low elevation regions. The different variation characteristics of these low
93 clouds at different elevations and regions also need to be discussed and analyzed.
94 Moreover, we need to investigate whether there exists “high efficiency” triggering
95 mechanisms for convection over the TP, and whether there is an association among
96 low air density, strong turbulence and ubiquitous “popcorn-like” cumulus clouds. Is
97 there also strong turbulence at higher elevation regions with lower air density in the
98 globe? What is the impact of the large scale vertical motions on clouds? Because both
99 the TP and Rocky Mountains are high elevation regions covering large mid-latitude
100 areas, we select these two typical regions to make a deep analysis. Unlike our
101 previous paper by Wang et al. (2020), in this study we mainly focus on the
102 comparison between these two regions to analyze the above scientific questions.

103 **2 Observational and reanalysis data**

104 We use in situ measurements of temperature (T) and relative humidity (RH) at 2
105 m height, surface pressure data every hour, and low cloud cover (LCC) every three
106 hours from 2402 automatic weather stations from June to August of 2010-2019 in
107 China. LCC here refers to the fraction of the sky covered by low clouds as estimated
108 by human observers, including five cloud types: nimbostratus (Ns), stratocumulus
109 (Sc), stratus (St), cumulus (Cu), and deep convection (DC). These surface observation
110 datasets are provided by China National Meteorological Information Center.

111 In addition, we use the hourly $0.25^\circ \times 0.25^\circ$ ERA5 reanalysis surface-layer data
112 in summer (June 1 to August 31) from 2010 to 2019 (Hersbach et al., 2020).

113 We use more than 4 years (from June 15 2006 to August 31 2010) of the satellite
114 (CloudSat radar and Calipso lidar)-merged cloud classification product
115 2B-CLDCLASS-lidar to calculate the mean LCC with $1^\circ \times 1^\circ$ resolution at about 2:00
116 pm and 2:00 am LT in summer. The introduction of this product and details of the
117 LCC calculation methods are summarized in Sassen and Wang (2008) and Wang et al
118 (2020).

119 We use a Gaofen 4 (GF 4) visible satellite image with a spatial resolution of 50 m
120 on August 4 of 2020 to show the organized structures (cellular convection) in
121 southeastern TP, as shown in Figure 1. GF 4 is a geostationary earth observation
122 satellite in the Gaofen series of Chinese civilian remote sensing satellites. We also use

123 the 1 year (from June 1 to August 31 of 2016) geostationary satellite Himawari-8
 124 retrieval product (cloud top height) over land in East Asia.

125 In this study, we also use temperature (T) at 2 m height, relative humidity (RH) at
 126 2 m height, surface pressure and planetary boundary layer height (PBLH) from ERA5
 127 reanalysis data from 2010 to 2019. To be specific, the above four variables represent
 128 hourly averaged values for each month (24 values in total for a month). The lifting
 129 condensation level (LCL) is calculated by the method proposed by (Romps, 2017).

130 Using sensible heat flux H , Northward turbulent surface stress τ_y and Eastward
 131 turbulent surface stress τ_x from ERA5 reanalysis data, we calculate the buoyancy term
 132 (BT) $(g/\theta_v \overline{w'\theta'_v})$ and shear term (ST) $(-\partial\bar{u}/\partial z \overline{u'w'})$ in the TKE equation for each grid.
 133 Both of these two terms can be used to analyze the effect of boundary layer
 134 turbulence in surface layer on convection. The details of the method for computing
 135 BT and ST are as follows:

136 The shear term (ST) $(-\partial\bar{u}/\partial z \overline{u'w'})$ and buoyancy term (BT) $(g/\theta_v \overline{w'\theta'_v})$ in the
 137 TKE equation maintain the turbulent motions. In order to simplify calculations, the
 138 x-axis is directed along the average wind. Assuming horizontal homogeneity and no
 139 mean divergence, the TKE equation is written as

$$140 \quad \frac{\partial \bar{e}}{\partial t} = \frac{g}{\theta_v} \overline{w'\theta'_v} - \overline{u'w'} \frac{\partial \bar{u}}{\partial z} - \frac{\partial(\overline{w'e})}{\partial z} - \frac{1}{\rho} \frac{\partial(\overline{w'p'})}{\partial z} - \varepsilon. \quad (1)$$

141 The left side of eq. (1) is the local time variation $\partial\bar{e}/\partial t$, and the terms on the
 142 right-hand side of eq. (1) describe the buoyancy and shear energy production or
 143 consumption, turbulent transport of \bar{e} , pressure correlation and viscous dissipation
 144 (Stull, 1988).

145 Here we use eq. (2) to calculate the virtual potential temperature θ_v , and $\overline{w'\theta'_v}$ is
 146 derived from eq. (3). Finally, we derive BT.

$$147 \quad \theta_v = T(1 + 0.608q) \left(\frac{p_0}{p} \right)^{\frac{R}{c_p}}, \quad (2)$$

$$148 \quad H = \rho c_p \overline{w'\theta'_v}, \quad (3)$$

149 Where $g = 9.8 \text{ m s}^{-2}$ is the gravitational constant, and $H \text{ (W m}^{-2}\text{)}$ is the sensible
 150 heat flux, $\rho \text{ (kg m}^{-3}\text{)}$ is the air density, R is the specific gas constant for dry air, c_p
 151 $(=1004 \text{ J kg}^{-1} \text{ K}^{-1})$ is the specific heat of air at constant pressure, T is the air
 152 temperature at 2 m height, q is the specific humidity at 2 m height, p_0 and p are
 153 standard atmospheric pressure and surface pressure, respectively.

154 The wind shear is determined from heat flux H and momentum flux τ obtained
 155 from the ERA5 reanalysis data. Because we cannot directly obtain the τ from ERA5
 156 product list, we need to use eq. (4) to calculate τ .

$$157 \quad \tau = \sqrt{\tau_x^2 + \tau_y^2}, \quad (4)$$

158 According to Monin Obukhov similarity theory wind shear is given as

$$159 \quad \frac{\partial \bar{u}}{\partial z} = \phi_m(\zeta) \frac{u_*}{\kappa z}, \quad (5)$$

160 Where ϕ_m is the Monin Obukhov stability function for momentum, $u_*^2 = \tau/\rho$.

161 The von Karman constant $\kappa=0.4$, \bar{u} is the horizontal wind speed in the surface
162 layer.

163 $\zeta = z/L$ with $z =$ height and $L =$ Obukhov stability length defined as in Gryanik et
164 al. (2020) as

$$165 \quad \zeta = \frac{z}{L}, L = -\frac{(\tau/\rho)^{3/2}}{\kappa(g/\theta_v)(H/\rho c_p)}. \quad (6)$$

166 ϕ_m is the Monin Obukhov stability function, here we use eq. (7) and eq. (8) for
167 stable and unstable conditions to derive ϕ_m (Dyer, 1974),

$$168 \quad \phi_m = 1 + 5\zeta, (\zeta > 0) \quad (7)$$

$$169 \quad \phi_m = (1 - 16\zeta)^{-1/4}, (\zeta < 0) \quad (8)$$

170 Then we use eq. (9) to derive $-\overline{u'w'}$. Finally, we derive ST.

$$171 \quad \overline{u'w'} = -\tau/\rho. \quad (9)$$

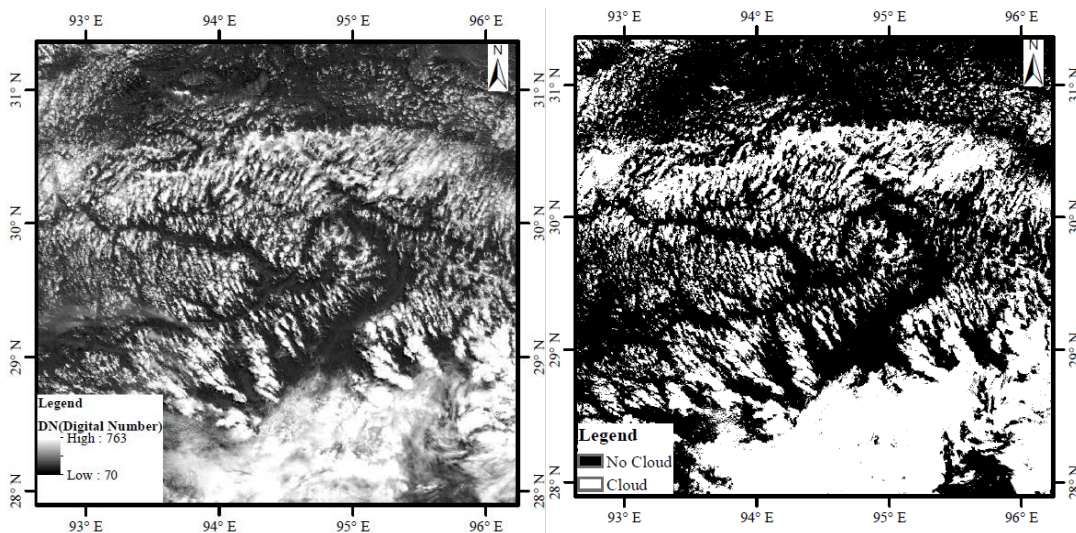
172

173 3 Results

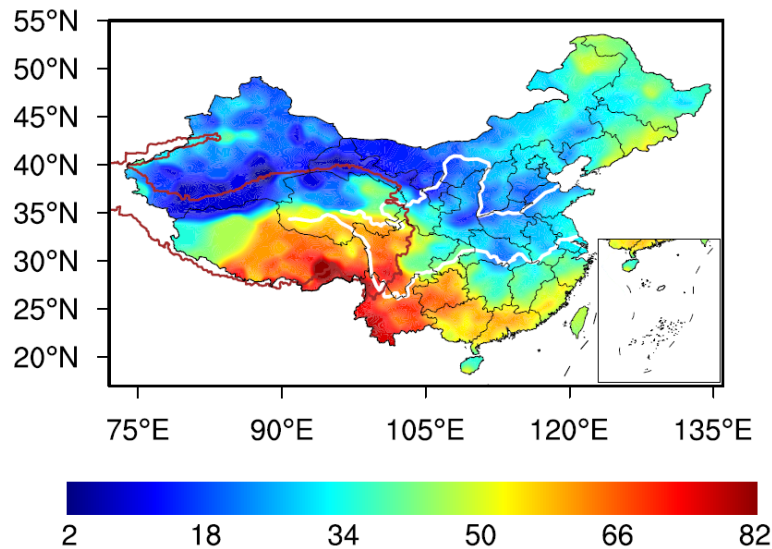
174 Figure 2 shows the spatial distribution of over-land low cloud cover (LCC) in
175 China from June to August of 1951-2019. Compared to the low LCC in eastern China,
176 the high value areas of LCC are mainly located in the mid-eastern TP and the area of
177 the upper Yangtze River Valley. But low LCC is also identified in western and
178 northern parts of TP. We will make a further discuss about it in subsequent paragraphs.
179 Using four years of CloudSat-Calipso satellite data, Li and Zhang (2016) confirmed
180 that the climatological occurrence of cumulus over the TP is significantly greater than
181 that in mid-eastern China on the same latitude. The elevated land surface with strong
182 radiative heating makes the massive TP a favorable region for initiating convective
183 cells with a high frequency of cumulonimbus and mesoscale convective systems
184 (Sugimoto and Ueno, 2012). As a strong heat source, the TP has frequent convective
185 activities in summer. During the TIPEX II in 1998, the long and narrow thermal
186 plume corresponding with vigorous cellular convection on micro-scale was observed
187 by sodar in Dangxiong. As shown in Figure 1, the shallow convective clouds on a
188 horizontal scale from hundreds of meters to several kilometres over the southeastern
189 TP (92.7-96.2E, 29.5-31.3N) are probably related to the organized eddies on the
190 meso-scale and micro-scale over the TP. The cloud fraction over the southeastern TP
191 is about 31.3%.

192 As shown in Figure 3, in general, LCC increases with increasing elevation. The
193 median of LCC_H is significantly greater than those of LCC_L and LCC_M throughout the
194 day. The diurnal variations of LCC_L and LCC_M are generally distributed in unimodal
195 pattern, with the maximum appearing at 2:00 pm Beijing time (median $LCC_L = 37\%$,

196 $LCC_M = 38\%$) and low values ($\sim 20\%$) are maintained during the night. The diurnal
 197 variation of LCC_H presents a bimodal curve with the maximum appearing at 5:00 pm
 198 Beijing time (median $LCC_H = 69\%$) and the secondary local maximum appearing at
 199 8:00 am Beijing time (median $LCC_H = 61\%$). Compared to the low elevation, the
 200 interquartile ranges (IQRs) of LCC_H are smaller than those of LCC_L and LCC_M ,
 201 which imply the LCC_H maintains high values during the day. To further confirm and
 202 compare the above results with in situ measurements, using ERA5 LCC data, we also
 203 add Figure S1 to show the diurnal cycle of LCC in summer in East Asia and North
 204 America in the supplementary material.

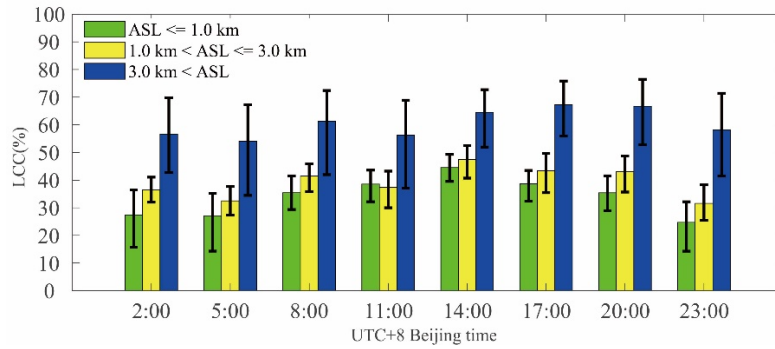


205
 206 Figure 1. The (a) digital number (DN) and (b) spatial distribution of cloud in
 207 southeastern TP from geostationary earth observation satellite Gaofen 4 (GF4) at
 208 12:00 pm Beijing time (about 10:20 am local time) on August 4 of 2020. Here we
 209 simply use $DN = 250$ as a threshold. All the grids in Figure (a) are divided into two
 210 classes ($DN > 250$, cloud; $DN < 250$, no cloud), and then we give Figure (b).



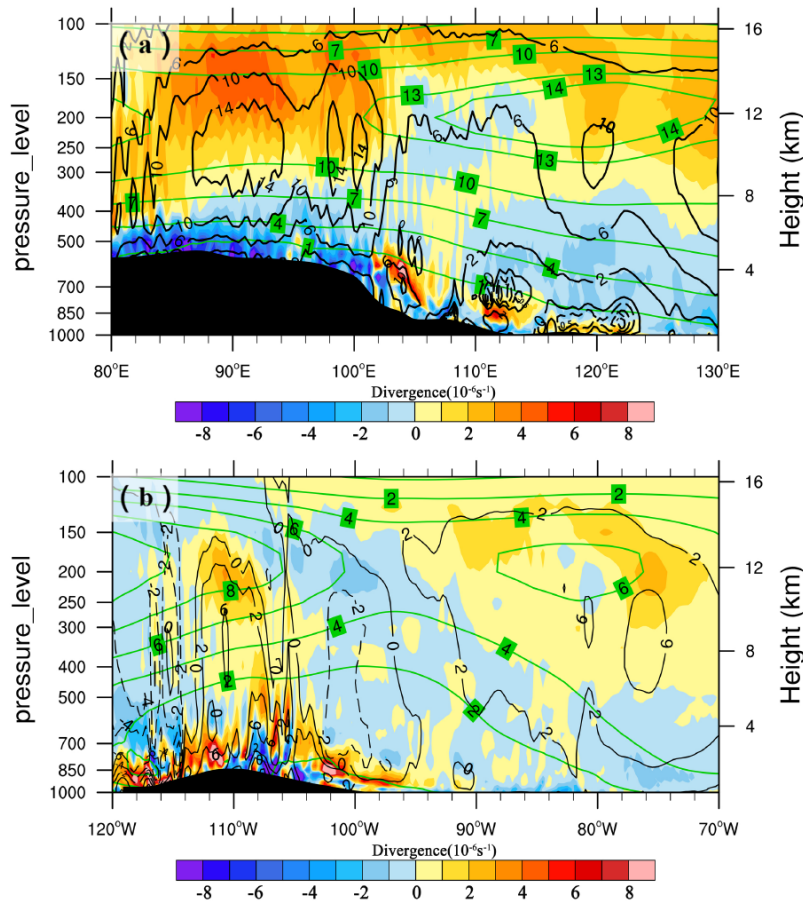
211
 212 Figure 2. The summer mean LCC derived from surface observations from 1951 to
 213 2019 in China. The thick

214 red contour denotes the 2.5 km topography height referred to as the TP. The white
 215 lines located in northern and southern parts of China denote the Yellow and Yangtze
 216 River, respectively.



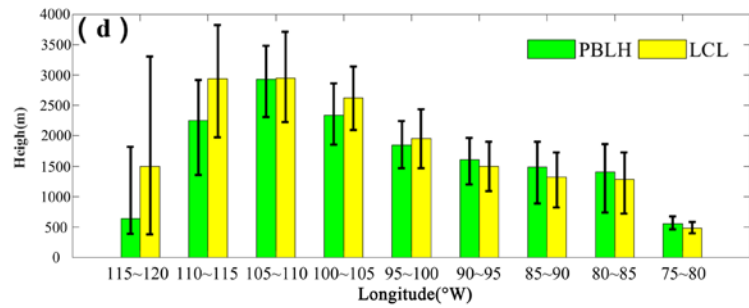
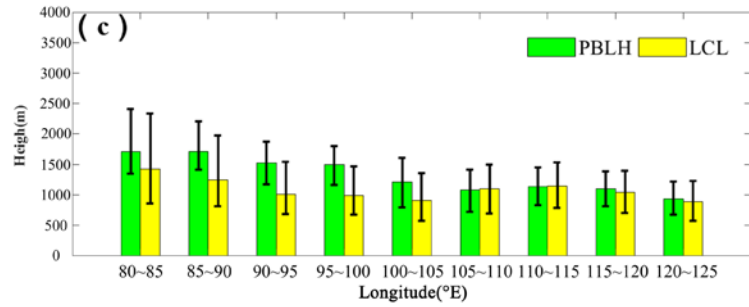
217
 218 Figure 3. The diurnal cycle of LCC in summer from 2010 to 2019 at different
 219 altitudes above sea level (ASL): $ASL \leq 1.0$ km (LCC_L), 1.0 km $< ASL \leq 3.0$ km
 220 (LCC_M), and 3.0 km $< ASL$ (LCC_H). It should be noted that all the sites are ranged
 221 from 27N to 40N in China, and each sample is derived from monthly mean LCC at a
 222 particular time in summer for each site. The bar and error bar represent the median
 223 values and interquartile ranges (IQRs) of LCC, respectively. The subscripts L, M and
 224 H of LCC denote the low, median and high clouds, respectively.

225
 226



227

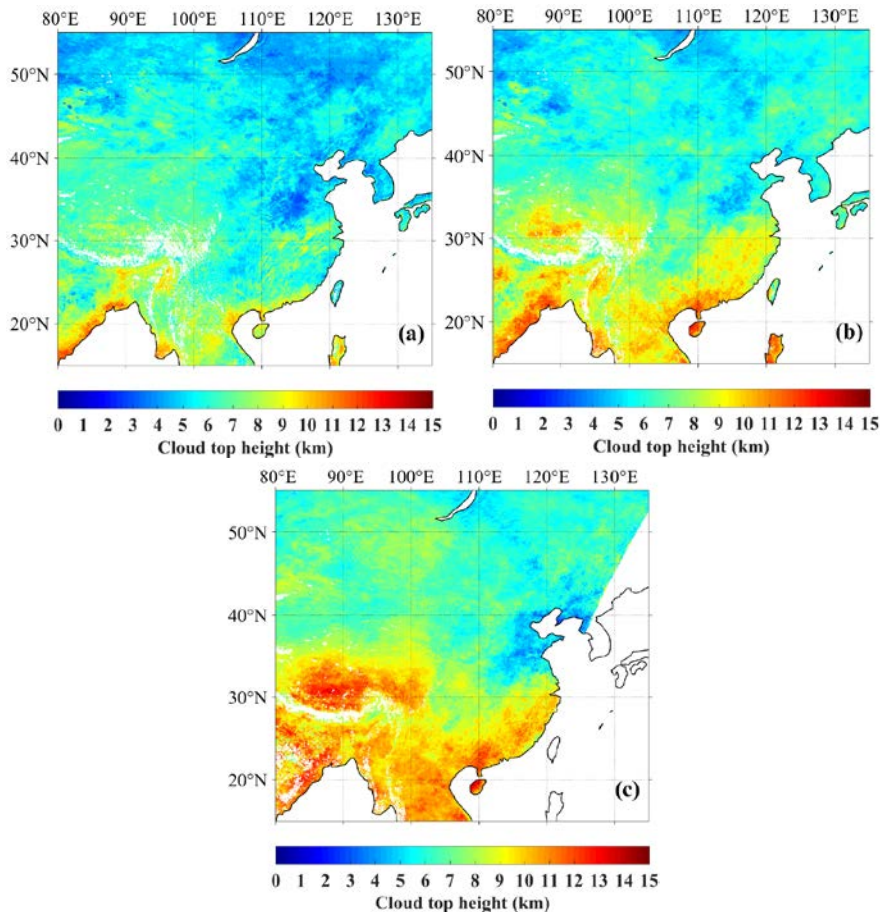
228



229

230

231 Figure 4. Vertical distribution of summer mean divergence (10^{-6} s^{-1}) (shaded) at 2:00
 232 pm local time from 2010 to 2019 at the latitude across sections from 30N to 35N in (a)
 233 East Asia and (b) North America. The green and black contours denote the summer
 234 mean U- (m s^{-1}) and W- (10^{-2} m s^{-1}) wind components with the zonal circulations,
 235 respectively. The solid and dashed contour lines represent the positive and negative
 236 values, respectively. The black shaded areas represent topography. Figure (c) and (d)
 237 are the PBLH (green) and LCL (yellow) versus longitude in East Asia and North
 238 America, respectively. The bar and error bar represent the median values and
 239 interquartile ranges (IQRs), respectively.



240

241

242 Figure 5. The median cloud top height derived from the Himawari-8 retrieval product
 243 at three Beijing times: (a) 2:30 pm±0.5h (b) 4:30 pm±0.5h (c) 6:30 pm±0.5h from
 244 June to August in 2016 over land in East Asia. Missing data are shaded in white color.
 245

246

247

248

249

250

251

252

253

254

255

256

257

258

259

260

261

262

263

On the other hand, we note that, there is no obvious trend of decreasing LCC over the TP from late afternoon to evening as shown in Figure 3. Based on the spatial distribution of topography in the Northern Hemisphere as shown in Figure 7 (a), it is clear that both the TP (27-40N, 70-105E) and Rocky Mountains (27-40N, 103-120W) in North America are two large areas with high elevations in mid-latitude regions in the Northern Hemisphere, so here we select these two typical large topography regions to analyze the triggering effects of large topography and related dynamical structure within the boundary layer on convective clouds. As shown in Figure 4 (a), in general, there are obvious large scale ascending motions from middle troposphere (~500 hPa) to upper troposphere (~200 hPa) over the TP. The convergence in the middle troposphere (the blue shaded areas) and the divergence in the upper troposphere (the orange shaded areas) are usually associated with the deep convection over the TP. Figure 4 (c) shows there are generally positive PBLH-LCL (~500 m) over the TP, and the median and IQR of PBLH are close to those of LCL in East China. These results are consistent with the conclusions proposed by Xu et al. (2014) and Wang et al. (2020). In contrast, Figure 4 (b) shows there are only weak large scale ascending motions from near surface layer to the middle troposphere over the Rocky Mountains. The large-scale subsidence on both sides of the Rocky Mountains

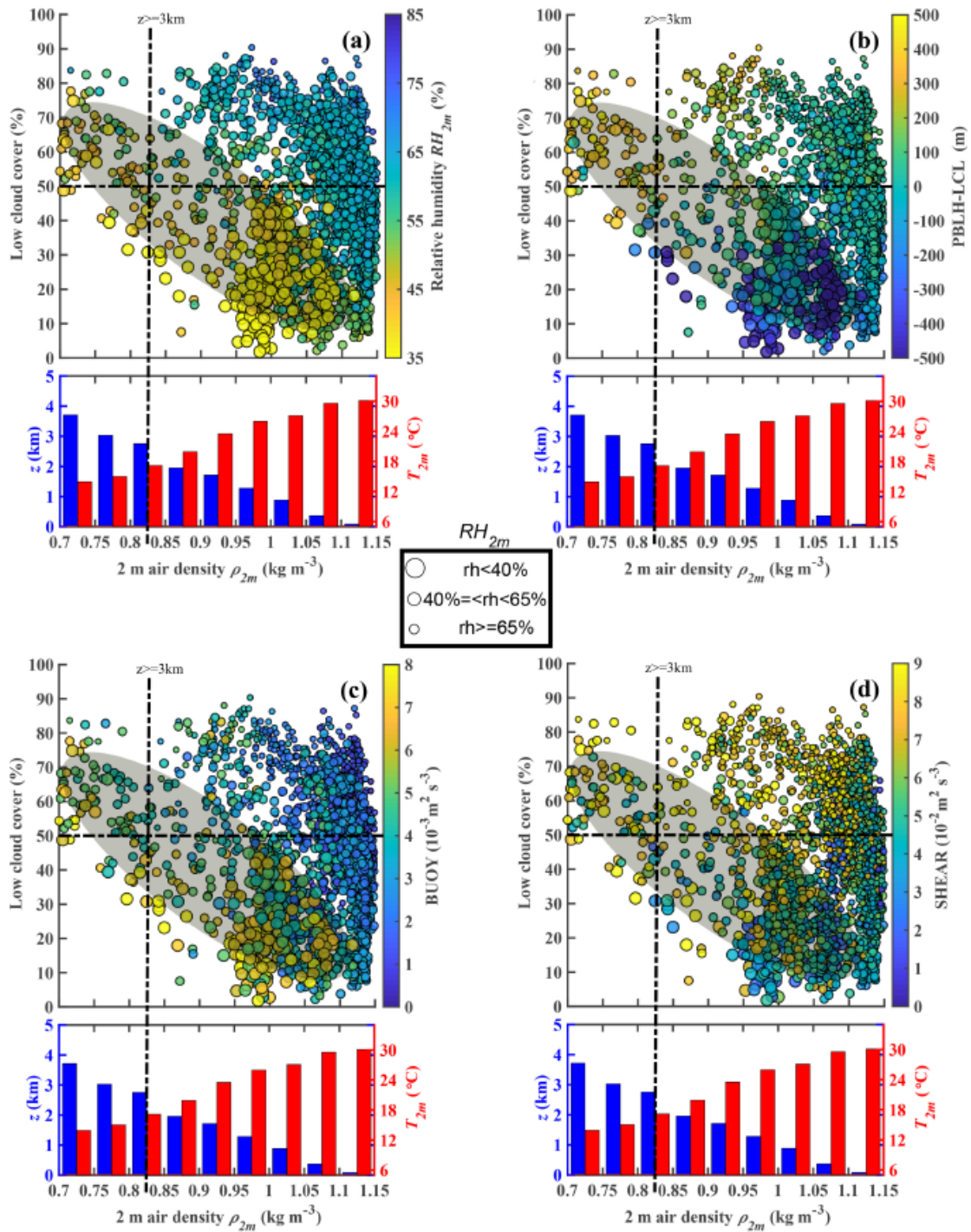
264 especially the western side can lead to inversion above PBL and lower RH within the
265 PBL, which can be verified by the vertical distribution of the $d\theta_v/dz$ and RH at the
266 latitude across sections from 30N to 35N over the Rocky Mountains in Figure S2.
267 There exists a high value center of $d\theta_v/dz$ at about 950 hPa (or 850 hPa) on western
268 (or eastern) side of the Rocky Mountains, and the RH within the PBL is generally less
269 than 55%. The former restricts the growth of PBLH during the day, while the latter
270 leads to an increased LCL. Thus, negative PBLH-LCL is identified on both sides of
271 the Rocky Mountains (30-35N, 110-120W and 30-35N, 100-105W), especially for the
272 western Rocky Mountain (30-35N, 110-120W) with strong large-scale subsidence, as
273 shown in Figure 4 (d). Dynamic processes of vapor transport are generated because of
274 the thermal structure of the TP, which is similar to the conditional instability of the
275 second kind (CISK) mechanism of tropical cyclones (Smith, 1997). It should be
276 pointed out that there are large scale descending motions at 500 hPa in part of the
277 western TP and Qaidam Basin as shown in Figure S3, which lead to less LCC in these
278 regions compared to the other parts of the TP, as shown in Figure 2. In addition, the
279 meteorological stations in the northern TP (34-36N, 80-90E) are scarcely and
280 unevenly distributed, and therefore the low LCC in the Taklamakan Desert leads to
281 false low LCC values in the northern TP (80-90E, 34-36N), as shown in Figure 2. In
282 fact, there are high LCC in these regions as shown in Figure 7 (e). Figure 5 shows the
283 spatial distribution of day time variations of cloud top height in summer. Compared to
284 eastern China at the same latitude, the cloud top height increases significantly from
285 2:30 pm (~7 km) to 6:30 pm (~14 km) over the TP. The cloud top height approaches
286 the tropopause (~14 km) in the evening, which implies the frequent occurrence of
287 deep convective clouds at this time. This result is consistent with the observation of
288 millimeter-wave radar in Naqu (Yi and Guo, 2016).

289 By comprehensively analyzing the TIPEX II sodar data, Xu et al. (2002) and
290 Zhou et al. (2000) found that, with narrow upward motion and time scale from 1.2 h
291 to 1.5 h, the maximum upward motion of the thermal turbulence was identified at the
292 height of about 120 m above the surface, with the vertical speed up to 1 m s^{-1} . They
293 also found symmetrical and wide downward motion areas on either side of the narrow
294 upward motion zone. The question arises as to whether there is a relationship between
295 the formation and evolution of frequent "pop-corn-like" convective clouds and
296 micro-scale thermal turbulence in the atmospheric convective boundary layer over the
297 TP. Xu et al., (2012) speculate these low clouds are probably initiated by strong
298 thermal turbulence under low air density conditions. Compared to the low elevation in
299 eastern China, the increased thermal turbulence associated with low air density over
300 the TP leads to the different turbulence characteristics of the convective boundary
301 layer (CBL). The CBL is mainly driven by buoyancy heat flux, and the thermal
302 turbulence with organized thermal plume is not totally random (Young, 1988a; Young,
303 1988b). The strong BT and ST over the TP play key roles in the convective activities
304 in lower troposphere.

305 By using the statistical results from sodar data in the TIPEX II, Zhou et al. (2000)
306 calculated the BT and ST at the height of 50 m under strong convection conditions in
307 Dangxiong (located at central TP). The results indicate that the BT is comparable to

308 ST. Both the thermodynamic and dynamic processes have important influences on the
309 convective activities. Both the BT and ST in the surface layer in Dangxiong are
310 almost an order of magnitude greater than those at low elevation given by Brummer
311 (1985) over North Sea and Weckwerth et al. (1997) in Florida. Direct measurements
312 from the Third Tibetan Plateau Experiments (TIPEX III) also confirmed that surface
313 buoyancy flux over the TP is significantly larger than that in eastern China (Zhou,
314 2000; Wang et al., 2016). Both the sodar data in TIPEX II and boundary layer tower
315 data in TIPEX III showed contributions of BT and ST to the turbulent kinetic energy
316 in the lower troposphere are larger over the TP than over the southeastern margin of
317 the TP and the low-altitude Chengdu Plain (Zhou, 2000; Wang et al., 2015). Thus one
318 might ask the question what is the relationship between high frequent low cloud and
319 the above physical quantities (e.g. turbulence structure, temperature and humidity)
320 under low air density conditions over the TP? The physical mechanism should be
321 discussed and analyzed. In addition, at low elevation in eastern China, the question
322 arises as to whether or not the variations of PBLH and LCL favor the formation and
323 development of low clouds.

324 As shown in Figure 6 (a), compared to the low elevation, there is larger LCC
325 ($LCC > 50\%$) over the TP ($ASL > 3$ km) under low RH_{2m} condition ($RH_{2m} < 40\%$). In
326 contrast, larger LCC mostly corresponds to higher RH_{2m} condition at low elevation,
327 which is consistent with our common sense. The above interesting phenomenon can
328 be explained by the differences of PBLH-LCL between the TP and low elevation
329 regions on summer afternoons. These differences are mainly attributed to following
330 two mechanisms. The first mechanism is that, with a similar sensible heat flux, the
331 lower air density over the TP leads to greater surface buoyancy flux (or BT) as shown
332 in Figure 6 (c), which is conducive to the increase of PBLH over the TP. Figure 6 (d)
333 shows great ST over the TP, which is mainly attributed to large wind speed. Although
334 here we only show the ST in the surface layer, strong wind shear in the boundary
335 layer probably also plays a role in increasing PBLH over the TP. On the other hand,
336 the second mechanism is that, with a similar RH, Wang et al. (2020) have indicated
337 that, compared to the low elevation in eastern China, the lower temperature over the
338 TP leads to a lower LCL. Together these two mechanisms lead to a greater
339 (PBLH-LCL) difference over the TP on summer afternoons, which increases the
340 probability of air parcels reaching the LCL and forming clouds as shown in Figure 6
341 (b). In most cases, the positive value of PBLH-LCL as well as the great BT and ST
342 over the TP corresponds with larger LCC ($LCC > 50\%$) under low RH_{2m} condition
343 ($RH_{2m} < 60\%$), which implies the enhanced local LCC is relevant to the diurnal
344 variation of the PBL process. In contrast, for the eastern China, in most cases, the
345 increased LCC ($LCC > 50\%$) generally corresponds with high RH_{2m} ($RH_{2m} > 60\%$),
346 and the LCC is not significantly correlated with PBLH-LCL or BT and ST, which
347 implies the other factors besides the PBL process (e.g. large scale ascending motion)
348 play a more important in LCC.



350

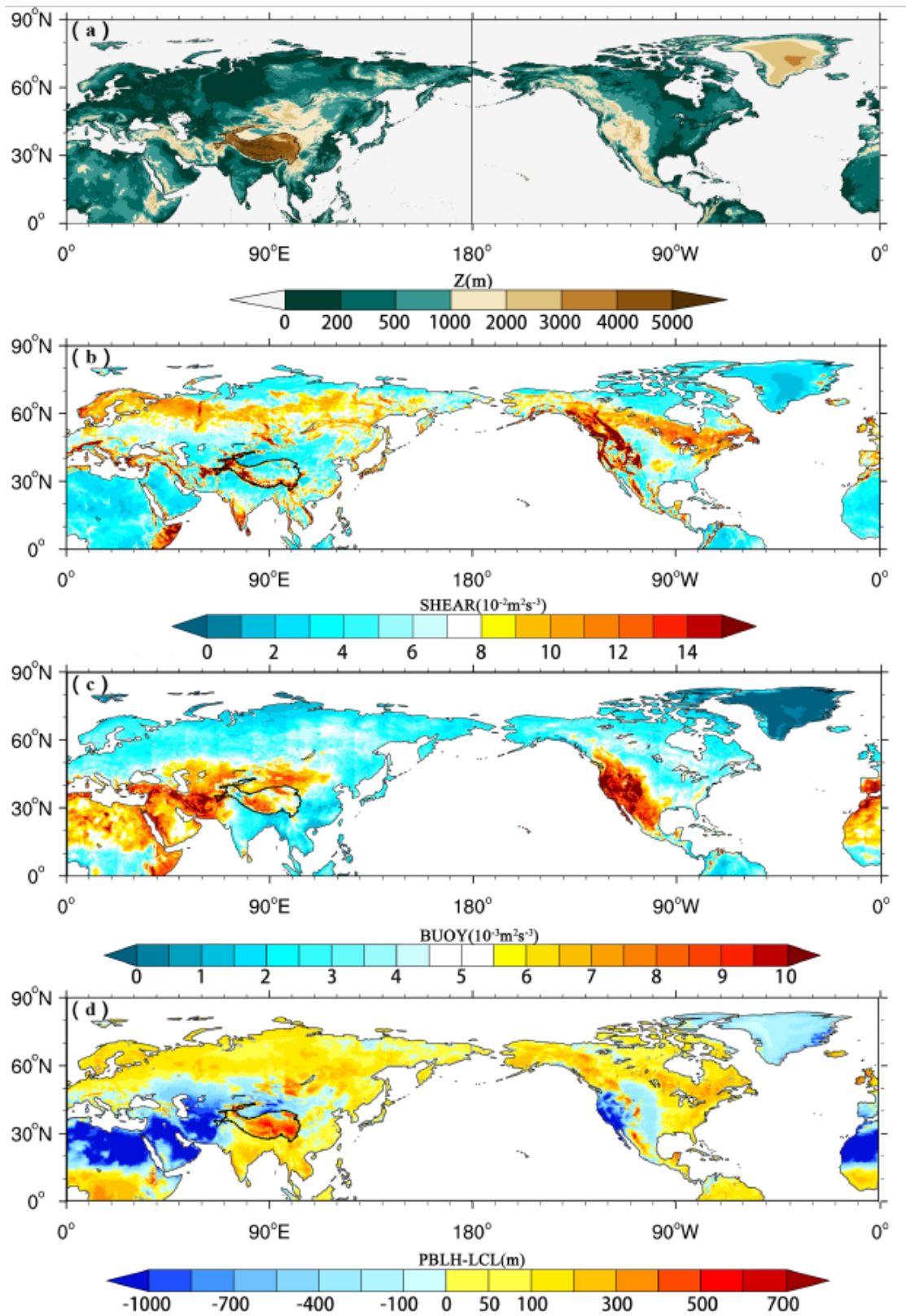
351 Figure 6. The relationships among monthly means of low cloud cover LCC, ρ_{2m} and
 352 (a) RH_{2m} , (b) PBLH-LCL, (c) BT and (d) ST at 2:00 pm Beijing time from 2010 to
 353 2019 in summer in China. The samples are divided into three groups: $RH_{2m} \geq 60\%$
 354 (small size dots), $60\% > RH_{2m} \geq 40\%$ (median size dots) and $RH_{2m} < 40\%$ (large
 355 size dots). The LCC, T_{2m} and RH_{2m} are observed by in situ measurements, and PBLH,
 356 LCL, BT and ST are derived from ERA5 reanalysis data. Here we use the nearest
 357 neighbor gridding method to derive PBLH, LCL, BT and ST at each site. The blue
 358 and red histograms show the surface elevation z (blue) and air temperature at 2 m (T_{2m})

359 (red) as functions of 2 m air density (ρ_{2m}). The dots with lower RH_{2m} ($RH_{2m} < 40\%$)
360 are mostly distributed within grey shaded elliptic regions as shown in Figure 6 (a)-(d).

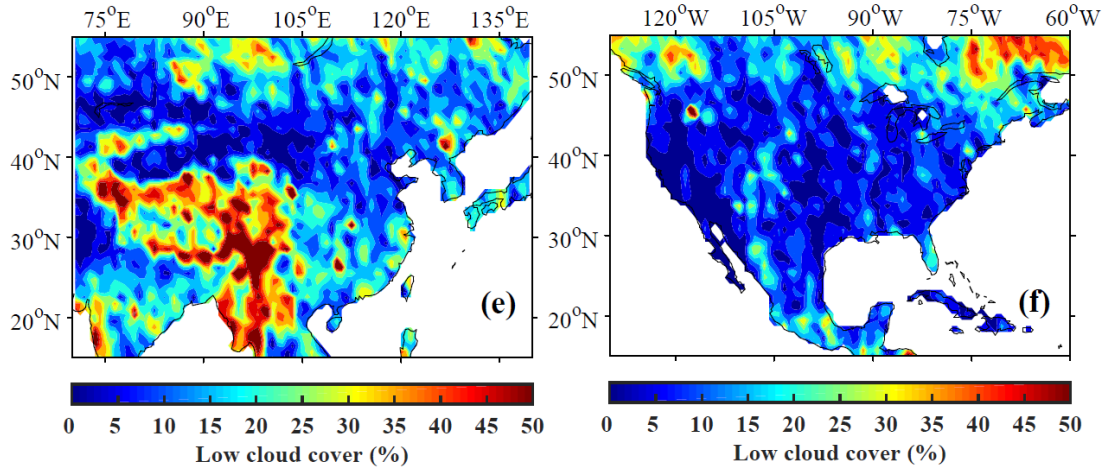
361 Figure 7 (d) shows the mean spatial distribution of PBLH – LCL in the Northern
362 Hemisphere from June to August of 2010-2019. The TP (27-40N, 70-105E) and
363 Rocky Mountains (27-40N, 103-120W) are two typical large topography regions in
364 the Northern Hemisphere, and the mean PBLH – LCL over the TP and Rocky
365 Mountains are 376.7 m and -101.9 m, respectively.

366 Figure 7 (b)-(c) shows the spatial distribution of ST and BT in the Northern
367 Hemisphere from June to August of 2010-2019, respectively. The effect of strong
368 thermal turbulence results in obvious positive values of PBLH – LCL at high
369 elevation regions under low air density conditions in the Northern Hemisphere (BT =
370 $0.008 \text{ m}^2 \text{ s}^{-3}$, PBLH – LCL = 376.7 m over the TP and BT = $0.011 \text{ m}^2 \text{ s}^{-3}$, PBLH –
371 LCL = -101.9 m over the Rocky Mountains). Figure 7 (b) also shows that there are
372 strong STs at these two high elevation regions (ST = $0.087 \text{ m}^2 \text{ s}^{-3}$ over the TP and ST
373 = $0.085 \text{ m}^2 \text{ s}^{-3}$ over the Rocky Mountains). Both the BT and ST increase significantly
374 at high elevation due to low air density compared to those at low elevation. The above
375 results enlighten us on thinking about whether the triggering effects of large
376 topography and boundary layer turbulence, which reflect the special surface
377 characteristics in the boundary layer at high elevation regions under low air density
378 conditions, can be applicable for any large topography in the globe, including TP and
379 other regions (e.g. Rocky Mountains).

380 Figure 8 shows a conceptual model of the atmosphere from the near-surface to
381 upper troposphere over the TP. Compared to the low elevation, the TP is characterized
382 by higher PBLH and lower LCL because of strong BT and ST, which is favorable for
383 the formation of shallow clouds in the afternoon. Meanwhile, the large scale
384 ascending motion over the TP results in the transition from shallow clouds to deep
385 convective clouds in the late afternoon and evening.

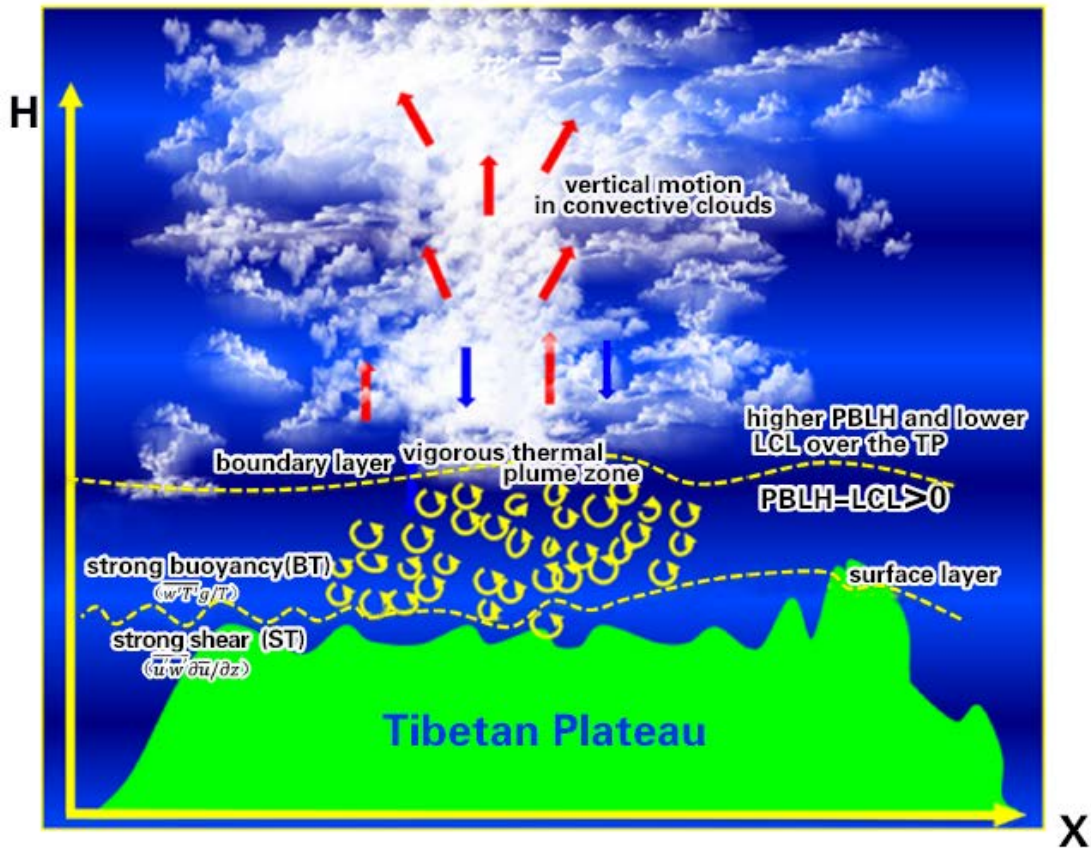


386



387

388 Figure 7. The spatial distribution of (a) ground level elevation (m), (b) ST ($10^{-2} \text{ m}^2 \text{ s}^{-3}$),
 389 (c) BT ($10^{-3} \text{ m}^2 \text{ s}^{-3}$), and (d) PBLH-LCL (m) derived from ERA5 reanalysis data at
 390 local time 2:00 pm in the Northern Hemisphere in summer. Figure (e) and (f) are the
 391 summer mean LCC (%) derived from cloudsat satellite data at local time 2:00 pm in
 392 eastern Asia and North America, respectively.



393

394

395

Figure 8. The characteristics model of boundary layer turbulence related to “high efficiency” triggering mechanisms for convection over the TP.

396 **4 Conclusions and further discussion**

397 In this study, we focus on the triggering effects of large topography and boundary
398 layer turbulence over the Tibetan Plateau on convection. The topography of the TP
399 plays a major role in the increased occurrences of convective clouds. Our results
400 further confirm the conclusions from Wang et al. (2020), which found that the
401 difference PBLH-LCL in the summer afternoon over the TP is greater than that in
402 eastern China. Compared to the eastern China, with the same relative humidity, lower
403 temperature over the TP results in a lower lifting condensation level. With the same
404 surface sensible heat flux, lower air density over the TP results in a larger buoyancy
405 flux and a deeper boundary layer. The observational results show that, under low
406 relative humidity condition ($RH < 40\%$), the low cloud cover (LCC) is higher than 60%
407 over the TP. In contrast, the high LCC ($LCC > 60\%$) only appears under high RH
408 condition ($RH > 60\%$) at low elevation.

409 In general, LCC increases with increasing elevation. The median of LCCs at high
410 elevation (TP) is significantly greater than those at low elevation (eastern China)
411 throughout the day. The diurnal variations of LCC at low elevation are generally
412 distributed in an unimodal pattern with the maximum appearing at 2:00 pm Beijing
413 time and low values during the night. The diurnal variations of LCC at high elevation
414 (TP) present a bimodal curve with the maximum appearing at 5:00 pm Beijing time
415 and the secondary local maximum appearing at 8:00 am Beijing time. In addition,
416 LCC maintains at high values at high elevation (TP) during the day. The median
417 cloud top height derived from Himawari-8 retrieval product shows the transition from
418 shallow clouds to deep convective clouds in the late afternoon and evening over the
419 TP, which is attributed to the strong large-scale ascending motion from the near
420 surface to upper troposphere over the TP.

421 The buoyancy term (BT) and shear term (ST) over the TP are significantly greater
422 than those at the low elevation, which is favorable for the increasing of PBLH.
423 Similar phenomena occur at other high elevation areas (e.g. Rocky Mountains). The
424 strong thermal turbulence and large scale ascending motion jointly results in positive
425 value of PBLH-LCL under low RH condition over the TP. The obvious large-scale
426 subsidence on both sides of the Rocky Mountain especially the western side leads to
427 inversion above PBL and lower RH within the PBL, which further lead to negative
428 value of PBLH-LCL and decreased LCC in most part of Rocky Mountain. The
429 slightly greater than zero PBLH-LCL corresponds spatially to increased LCC in the
430 partial regions of central Rocky Mountain. Thus less LCC is generated at the Rocky
431 Mountains compared to the TP.

432

433 **Data availability**

434 All reanalysis data used in this study were obtained from publicly available sources:
435 ERA5 reanalysis data can be obtained from the ECMWF public datasets web interface
436 (<http://apps.ecmwf.int/datasets/>). The satellite (CloudSat radar and Calipso
437 lidar)-merged cloud classification product 2B-CLDCLASS-lidar were obtained from

438 Colorado State University
439 (<http://www.cloudsat.cira.colostate.edu/data-products/level-2b/2b-cldclass-lidar>). The
440 Himawari-8 retrieval products were obtained from JAXA Himawari Monitor
441 (<https://www.eorc.jaxa.jp/ptree/>).

442 **Code Availability**

443 The data in this study are analysed with MATLAB and NCL. Contact Y.W. for specific
444 code requests.

445 **Acknowledgements**

446 Xu and Wang are supported by the Second Tibetan Plateau Scientific Expedition and
447 Research (STEP) program (Grant Nos. 2019QZKK0105), National Natural Science
448 Foundation of China (Grant Nos. 91837310), and the National Natural Science
449 Foundation for Young Scientists of China (Grant Nos. 41805006).

450 **Author Contributions**

451 X.X. and Y. W. led this work with contributions from all authors. Y.T. and Y. W.
452 made the calculations and created the figures. X.X., Y.W., H.Z. and M.Z. led analyses,
453 interpreted results and wrote the paper. R.L. supports high resolution satellite Gaofen
454 images to show the organized structures (cellular convection) for shallow convection.

455 **Competing interests**

456 The authors declare no competing interests.

457

458 **References**

459 Brümmer, B.: Structure, dynamics and energetics of boundary layer rolls from Kon
460 Tur aircraft observations, undefined, 1985.

461 Dyer, A. J.: A review of flux-profile relationships, *Bound.-Layer Meteorol.*, 7, 363–
462 372, <https://doi.org/10.1007/bf00240838>, 1974.

463 Ek, M. and Mahrt, L.: Daytime Evolution of Relative Humidity at the Boundary
464 Layer Top, *Mon. Weather Rev.*, 122, 2709–2721,
465 [https://doi.org/10.1175/1520-0493\(1994\)122<2709:DEORHA>2.0.CO;2](https://doi.org/10.1175/1520-0493(1994)122<2709:DEORHA>2.0.CO;2), 1994.

466 Findell, K. L. and Eltahir, E. A. B.: Atmospheric Controls on Soil Moisture–Boundary
467 Layer Interactions. Part I: Framework Development, *J. Hydrometeorol.*, 4, 552–569,
468 [https://doi.org/10.1175/1525-7541\(2003\)004<0552:ACOSML>2.0.CO;2](https://doi.org/10.1175/1525-7541(2003)004<0552:ACOSML>2.0.CO;2), 2003.

469 Flohn, H. and Reiter, E. R.: Contributions to a meteorology of the Tibetan highlands,
470 1967.

471

472 Gentine, P., Holtslag, A. A. M., D'Andrea, F., and Ek, M.: Surface and Atmospheric
473 Controls on the Onset of Moist Convection over Land, *J. Hydrometeorol.*, 14, 1443–
474 1462, <https://doi.org/10.1175/JHM-D-12-0137.1>, 2013.

475 Gryanik, V. M., Lüpkes, C., Grachev, A., & Sidorenko, D.: New modified and
476 extended stability functions for the stable boundary layer based on SHEBA and
477 parametrizations of bulk transfer coefficients for climate models. *J. Atmos. Sci.*, 77(8),
478 2687–2716, <https://doi.org/10.1175/JAS-D-19-0255.1>, 2020.

479 Guillod, B. P., Orlowsky, B., Miralles, D. G., Teuling, A. J., and Seneviratne, S. I.:
480 Reconciling spatial and temporal soil moisture effects on afternoon rainfall, *Nat.*
481 *Commun.*, 6, 6443, <https://doi.org/10.1038/ncomms7443>, 2015.

482 Hersbach, H., Bell, B., Berrisford, P., Hirahara, S., Horányi, A., Muñoz-Sabater, J.,
483 Nicolas, J., Peubey, C., Radu, R., Schepers, D., Simmons, A., Soci, C., Abdalla, S.,
484 Abellan, X., Balsamo, G., Bechtold, P., Biavati, G., Bidlot, J., Bonavita, M., Chiara, G.
485 D., Dahlgren, P., Dee, D., Diamantakis, M., Dragani, R., Flemming, J., Forbes, R.,
486 Fuentes, M., Geer, A., Haimberger, L., Healy, S., Hogan, R. J., Hólm, E., Janisková,
487 M., Keeley, S., Laloyaux, P., Lopez, P., Lupu, C., Radnoti, G., Rosnay, P. de, Rozum,
488 I., Vamborg, F., Villaume, S., and Thépaut, J.-N.: The ERA5 global reanalysis, *Q. J. R.*
489 *Meteorol. Soc.*, 146, 1999–2049, <https://doi.org/10.1002/qj.3803>, 2020.

490 Li, Y. and Zhang, M.: Cumulus over the Tibetan Plateau in the Summer Based on
491 CloudSat–CALIPSO Data, *J. Clim.*, 29, 1219–1230,
492 <https://doi.org/10.1175/JCLI-D-15-0492.1>, 2016.

493 Luo, Y., Zhang, R., Qian, W., Luo, Z., and Hu, X.: Intercomparison of Deep
494 Convection over the Tibetan Plateau–Asian Monsoon Region and Subtropical North
495 America in Boreal Summer Using CloudSat/CALIPSO Data, *J. Clim.*, 24, 2164–2177,
496 <https://doi.org/10.1175/2010JCLI4032.1>, 2011.

497 Romps, D. M. (2017). Exact expression for the lifting condensation level. *Journal of*
498 *the Atmospheric Sciences*, 74, 3891–3900. [https://doi.org/10.1175/JAS-D-17-](https://doi.org/10.1175/JAS-D-17-0102.1)
499 [0102.1](https://doi.org/10.1175/JAS-D-17-0102.1)

500 Sassen, K. and Wang, Z.: Classifying clouds around the globe with the CloudSat radar:
501 1-year of results, *Geophys. Res. Lett.*, 35, <https://doi.org/10.1029/2007GL032591>,
502 2008.

503 Smith, R. K.: On the theory of CISK, *Q. J. R. Meteorol. Soc.*, 123, 407–418, 1997.

504 Stull, R. B.: Mean Boundary Layer Characteristics, in: *An Introduction to Boundary*
505 *Layer Meteorology*, edited by: Stull, R. B., Springer Netherlands, Dordrecht, 1–27,
506 https://doi.org/10.1007/978-94-009-3027-8_1, 1988.

507 Sugimoto, S. and Ueno, K.: Role of Mesoscale Convective Systems Developed
508 around the Eastern Tibetan Plateau in the Eastward Expansion of an Upper

- 509 Tropospheric High during the Monsoon Season, *J. Meteorol. Soc. Jpn. Ser II*, 90,
510 297–310, <https://doi.org/10.2151/jmsj.2012-209>, 2012.
- 511 Taylor, C. M., de Jeu, R. A. M., Guichard, F., Harris, P. P., and Dorigo, W. A.:
512 Afternoon rain more likely over drier soils, *Nature*, 489, 423–426,
513 <https://doi.org/10.1038/nature11377>, 2012.
- 514 Tuttle, S. and Salvucci, G.: Empirical evidence of contrasting soil moisture–
515 precipitation feedbacks across the United States, *Science*, 352, 825–828,
516 <https://doi.org/10.1126/science.aaa7185>, 2016.
- 517 Wang, Y., Xu, X., Zhao, T., Sun, J., Yao, W., and Zhou, M.: Structures of convection
518 and turbulent kinetic energy in boundary layer over the southeastern edge of the
519 Tibetan Plateau, *Sci. China Earth Sci.*, 58, 1198–1209,
520 <https://doi.org/10.1007/s11430-015-5054-1>, 2015.
- 521 Wang, Y., Xu, X., Liu, H., Li, Y., Li, Y., Hu, Z., Gao, X., Ma, Y., Sun, J., Lenschow, D.
522 H., Zhong, S., Zhou, M., Bian, X., and Zhao, P.: Analysis of land surface parameters
523 and turbulence characteristics over the Tibetan Plateau and surrounding region, *J.*
524 *Geophys. Res. Atmospheres*, 121, 9540–9560, <https://doi.org/10.1002/2016JD025401>,
525 2016.
- 526 Wang, Y., Zeng, X., Xu, X., Welty, J., Lenschow, D. H., Zhou, M., and Zhao, Y.: Why
527 Are There More Summer Afternoon Low Clouds Over the Tibetan Plateau Compared
528 to Eastern China?, *Geophys. Res. Lett.*, 47, e2020GL089665,
529 <https://doi.org/10.1029/2020GL089665>, 2020.
- 530 Weckwerth, T. M., Wilson, J., Wakimoto, R., and Crook, N. A.: Horizontal convective
531 rolls: Determining the environmental conditions supporting their existence and
532 characteristics, *Mon. Weather Rev.*, 125, 505–526,
533 [https://doi.org/10.1175/1520-0493\(1997\)12560;0505:hcrdte62;2.0.co;2](https://doi.org/10.1175/1520-0493(1997)12560;0505:hcrdte62;2.0.co;2), 1997.
- 534 Wu, G., Duan, A., Liu, Y., Mao, J., Ren, R., Bao, Q., He, B., Liu, B., and Hu, W.:
535 Tibetan Plateau climate dynamics: recent research progress and outlook, *Natl. Sci.*
536 *Rev.*, 2, 100–116, <https://doi.org/10.1093/nsr/nwu045>, 2015.
- 537 Xu, X., Zhou, M., Chen, J., Bian, L., Zhang, G., Liu, H., Li, S., Zhang, H., Zhao, Y.,
538 Suolongduoji, and Jizhi, W.: A comprehensive physical pattern of land-air dynamic
539 and thermal structure on the Qinghai-Xizang Plateau, *Sci. China Ser. D*, 45, 577–594,
540 <https://doi.org/10.1360/02yd9060>, 2002.
- 541 Xu, X., Zhang, R., Koike, T., Lu, C., Shi, X., Zhang, S., Bian, L., Cheng, X., Li, P.,
542 and Ding, G.: A New Integrated Observational System Over the Tibetan Plateau, *Bull.*
543 *Am. Meteorol. Soc. - BULL AMER METEOROL SOC*, 89, 1492–1496,
544 <https://doi.org/10.1175/2008BAMS2557.1>, 2008.
- 545 Xu, X., Shi, X., and Lu, C.: Theory and application for warning and prediction of

546 disastrous weather downstream from the Tibetan Plateau, *Theory Appl. Warn. Predict.*
547 *Disastrous Weather Downstr. Tibet. Plateau*, 1–116, 2012.

548 Xu, X., Zhao, T., Lu, C., Guo, Y., Chen, B., Liu, R., Li, Y., and Shi, X.: An important
549 mechanism sustaining the atmospheric “water tower” over the Tibetan Plateau,
550 *Atmospheric Chem. Phys.*, 14, 11287–11295,
551 <https://doi.org/10.5194/acp-14-11287-2014>, 2014.

552 Yi, C., and Guo, X.: Characteristics of convective cloud and precipitation during
553 summer time at Naqu over Tibetan Plateau (in Chinese), *Chinese Science Bulletin*, 61,
554 1706–471, <https://doi.org/10.1360/N972015-01292>, 2016.

555 Young, G. S.: Convection in the atmospheric boundary layer, *Earth-Sci. Rev.*, 25,
556 179–198, [https://doi.org/10.1016/0012-8252\(88\)90020-7](https://doi.org/10.1016/0012-8252(88)90020-7), 1988a.

557 Young, G. S.: Turbulence Structure of the Convective Boundary Layer. Part I.
558 Variability of Normalized Turbulence Statistics, *J. Atmospheric Sci.*, 45, 719–726,
559 [https://doi.org/10.1175/1520-0469\(1988\)045<0719:TSOTCB>2.0.CO;2](https://doi.org/10.1175/1520-0469(1988)045<0719:TSOTCB>2.0.CO;2), 1988b.

560 Zhou, M., Xu, X., Bian, L., Chen, J., Liu H., Zhang, H., Li, S., and Zhao J.:
561 Observational analysis and dynamic study of atmospheric boundary layer on Tibetan
562 Plateau (in Chinese), 125 pp., 2000.

563